Heat Transfer Modelling of Gas-Liquid Slug Flow without Phase Change in a Micro Tube

Qunwu He [a,*] , Yosuke Hasegawa [b] , Nobuhide Kasagi [b]

[a] *Nuclear Safety Technology Research Center, Suzhou Nuclear Power Institute, China Guangdong Nuclear Power Group, China*
Xihuan Road 1788, Suzhou, 215004, China
Tel: +86-512-6860-2611.

[b] *Department of Mechanical Engineering, The University of Tokyo*
Hongo 7-3-1, Bunkyo-ku, Tokyo, 113-8656, Japan
Tel: +81-3-5841-6419; Fax: +81-3-5800-6999.

Abstract

Numerical simulation of gas-liquid slug flow and associated heat transfer without phase change in a micro tube is carried out. The presence of a gas bubble causes recirculating flow inside a liquid slug, and therefore enhances heat transfer. It is shown that the heat transfer rate is strongly dependent on the flow pattern, i.e., the slug length and the flow rate of each of gas and liquid. The whole flow field is modelled as an adherent liquid film, above which the gas and liquid slugs alternately pass. Since the heat capacity and conductivity of gas phase are negligibly small, while the liquid film is sufficiently thin, the overall heat transfer can be deduced as one-dimensional unsteady heat conduction inside the liquid film with a time-dependent heat transfer rate at the interface between the film and the slug regions. We propose a heat transfer model as a function of parameters representing the flow pattern and assess it in comparison with the present numerical results.

Key words: Two-phase flow, Micro tube, Heat Transfer, Slug flow

1 INTRODUCTION

Gas-liquid two-phase flow without phase change is a possible way of heat transfer enhancement for compact heat exchangers. The presence of gas bubbles separating discrete liquid slugs causes a circulation inside the liquid phase so that the overall heat transfer is enhanced. Moreover, such gas-liquid flows are rather stable due to an absence of explosive boiling. These facts open up a possibility of achieving better heat transfer with moderate pressure penalty. The structure and behavior of such tow-phase flow, however, are inherently complex, so that basic understanding the flow and heat transfer mechanisms is essential.

A number of experimental visualizations have been carried out in order to clarify the flow characteristics of adiabatic gas-liquid two-phase flow in micro tubes (Tripletter et al. 1999; Kawahara et al., 2002; Serizawa et al., 2002.). A thorough review has been provided by Ghiaasiaan and Abdel-khalik (2001). Recently, it has been shown that the flow pattern in a micro tube is not uniquely determined with the flow rates of gas and liquid, but strongly depends on the inlet condition. Once a flow pattern is reached downstream of the inlet, it remains unchanged even far downstream (Hayashi et al., 2007; Kawaji et al., 2009). These facts suggest a possibility to control the flow pattern so as to achieve favorable heat transfer characteristics by modifying the inlet condition.

Advanced numerical simulation provides an opportunity to obtain local velocity and temperature information to explore the underlying physics. However, the numerical simulation of two-phase flow in a micro conduit is not an easy

* Corresponding author.
Email addresses: qunwuhe@gmail.com (Qunwu He),
hasegawa@thtlab.t.u-tokyo.ac.jp (Yosuke Hasegawa),
kasagi@thtlab.t.u-tokyo.ac.jp (Nobuhide Kasagi).

task due to the dominant surface tension effect and the discontinuous change of fluid physical properties at the interface. He and Kasagi (2008a) found that the Phase-Field method coupled with the chemical potential formulation of the surface tension can significantly suppress the parasitic flow when simulating two-phase flow at small capillary numbers. This method was applied to study the pressure drop characteristics for bubbly and slug flows in a micro tube (He and Kasagi, 2008b). Concerning the heat transfer, Oliver and Hoon (1968) investigated the convective heat transfer of slug flows in a macro-sized tube by using viscoelastic fluids. Fukagata et al. (2007) simulated slug flows in a micro tube of 20μm ID and reported that the length of a bubble should considerably affect heat transfer characteristics.

One of the most fundamental problems is to predict the heat transfer rate based on the flow parameters, such as the slug lengths and flow rates of gas and liquid. A typical phenomenological models the three-zone flow boiling model proposed by Thome et al. (2003a & 2003b). They divide a gas-liquid slug flow into three zones, namely, liquid slug, elongated bubble and vapor slug. The overall heat transfer rate is given by the sum of the heat transfer rates multiplied by the transit-time fraction of each zone. Although this model has been successfully applied to boiling and condensation in a micro tube, there exists no model applicable to gas-liquid slug flow without phase change.

In the present work, we carry out a series of simulation of gas-liquid slug flow and associated heat transfer without phase change. Base on the numerical results, we decompose the whole flow field into an adherent liquid film near the wall and the gas-liquid slug regions. It is shown that the transient temperature fluctuation inside the liquid film is a key to predict the overall heat transfer rate. We analyze a one-dimensional transient heat conduction problem inside the liquid film, and then develop a heat transfer model as a function of parameters representing the flow pattern. Finally, we verify the present model

through comparison with the numerical results.

2 MATHEMATICAL FORMULATION

A gas-liquid two-phase flow in a cylindrical pipe is considered. It is assumed that each phase is incompressible and phase change does not take place. The temperature is considered as a passive scalar. The gravity is neglected due to dominance of the surface tension. The interface is captured by using the Phase-Field method (Anderson et al., 1998). The dimensionless governing equations are given as follows:

$$\nabla \cdot \vec{u} = 0, \tag{1}$$

$$\frac{\partial(\rho\vec{u})}{\partial t} + \vec{u} \cdot \nabla(\rho\vec{u}) = -\nabla p + \frac{1}{Re_{TP}} \nabla \cdot [\eta(\nabla\vec{u} + \nabla\vec{u}^T)] - \frac{\gamma}{Cn \cdot We} C \nabla f, \tag{2}$$

$$\frac{\partial C}{\partial t} + \vec{u} \cdot \nabla C = \frac{1}{Pe_C} \nabla^2 f, \qquad f = \Psi'(C) - Cn^2 \nabla^2 C, \tag{3}$$

$$\frac{\partial(\rho C_p T)}{\partial t} + \vec{u} \cdot \nabla(\rho C_p T) = \frac{1}{Pe_l} \nabla \cdot \lambda \nabla T, \tag{4}$$

where, ρ, μ, C_p and λ denote the density, viscosity, thermal capacity and conductivity, respectively, and all these quantities are normalized by the values of liquid. The relative concentration of liquid is denoted by C, where $C = 1$ represents liquid while $C = 0$ gas. The interface is expressed by a finite-thickness layer, where C changes from 0 to 1. The function of f is the dimensionless chemical potential, and $\Psi(C)$ is the bulk energy density defined as $C^2(1 - C^2)/4$ (Anderson et al., 1998).

The dimensionless parameters appear in Eqs. (2-4) are defined as:

$$Re_{TP} = \frac{\rho_l^* U_{TP}^* D^*}{\mu_l^*}, \quad We = \frac{\rho^* {U^*}_{TP}^2 D^*}{\sigma^*}, \quad Pe_C = \frac{U_{TP}^* D^*}{\mathcal{M}^* \mu^*}, \tag{5}$$

$$Pe_l = Re_{TP} Pr_l = \frac{\rho_l^* {C_{pl}}^* U_{TP}^* D^*}{\lambda_l^*}, Pr_l = \frac{\nu_l^*}{\alpha_l^*}, \quad Cn = \frac{\eta_\epsilon^*}{D^*}, \tag{6}$$

where a value with an asterisk denotes a dimensional quantity, while D^* is the tube diameter and the subscripts of l and g represent values in the liquid and gas phases, respectively. The thermal diffusion coefficient is denoted by $\alpha^* = \lambda^*/\rho^* C_p^*$. The characteristic velocity U_{TP}^* is defined as the sum of superficial liquid and gas velocities, i.e., $U_{TP}^* = j_g^* + j_l^*$.

Equations of (1) - (4) are satisfied both in gas and liquid phases, and the local fluid properties of ρ, μ, λ and C_p are interpolated between those of gas and liquid according to the position of interface. The details of the Phase-Field method can be found in Anderson et al. (1998).

The flow is assumed to be periodic with constant gas and liquid slug lengths. Therefore, only one period of the flow is simulated with a pair of gas and liquid slugs. In addition, the flow is assumed axisymmetric, so that a two-dimensional $(r - z)$ computational domain is employed. The periodic length $L_z = L_z^*/R^*$ defines the computation domain, where R^* is the tube radius. In the present study, L_z is changed as $3 \leq L_z \leq 15$ with different gas and liquid slug lengths. A periodic boundary condition is applied at the two ends of the computational domain, while the no-slip and fully wetted boundary conditions are used on the tube wall. For the temperature field, a uniform heat flux q is assumed along the wall. Because only the temperature difference is of interest, a quasi-periodic boundary condition, namely,

$$\frac{\partial T}{\partial z}\Big|_{z=0} = \frac{\partial T}{\partial z}\Big|_{z=L_z}, \tag{7}$$

is applied on the both ends of the computation domain.

In all calculations, the numbers of grid points N_r and N_z in the radial and axial directions are determined so as to keep the grid spacings below $\Delta z^*/R^* = \Delta z = 1/64$ and $\Delta r^*/R^* = \Delta r = 1/64$. For typical cases, we doubled the grid

numbers in the z and r directions, and have confirmed that the effects of grid resolution on the results shown here is sufficiently small for the purpose of the present investigation. More detailed verification will be discussed in the next section.

In accordance with the experiment by Hayashi et al. (2007), water and Nitrogen at 293 K and 1 atm are assumed as working fluids, and the surface tension σ^* is 0.0728 N/m. The tube diameter D^* is fixed at 600μm, and the characteristic velocity U^*_{TP} is given as 0.03$\sim$1.5m/s. This range covers both bubbly and slug flows according to experimental observation (Hayashi et al., 2007). The Prandtl number in liquid is $Pr_l = 6.96$ unless otherwise stated.

3 THERMAL HYDRAULICS CHARACTERISTICS

3.1 Velocity field

We consider a typical case, where $L_z = 6.0$ and the void fraction $\epsilon = 0.29$ as shown in Fig. 1. Three different grid systems of $(N_r, N_z) = (32, 192)$, $(64, 384)$ and $(128, 768)$ are employed. Figures 2 a, b) show the grid dependency of the axial velocity profiles at the front of bubble (FB) and the center of slug (CS), of which locations are indicated in Fig. 1.

Since the flow is laminar, the velocity profile converges fast and the result with radial grid resolution of $\Delta r = R/64$ almost coincides with that with $\Delta r = R/128$. In addition, the difference in the overall Nusselt number Nu_{TP} defined by Eq. (14) has also been found to be less than 1%. Therefore, we conclude that the grid resolution of $(\Delta r, \Delta z) = (64, 64)$ is fine enough to simulate the velocity and thermal fields for the present study.

As shown in Fig. 2 b), the velocity profile at the center of a liquid slug is close

to the parabolic profile of the single-phase laminar flow. The fluid at the tube center moves faster, while that close to tube wall moves slower due to the no-slip condition at the wall. When the fluid at the tube center approaches to the gas-liquid interface, it is decelerated to the interfacial convection velocity. Because of the immiscibility of the two phases, the bulk liquid impinges on the interface, and then changes its direction to the wall. Thus, a circulation is generated in the liquid slug. This is a primary reason for the heat transfer enhancement discussed below. More detailed analyses of the velocity field can be found in Fukagata et al. (2007).

To visualize the induced circulation, the contours of the dimensionless stream function ψ relative to the bubble motion are shown in Fig. 1. Here, ψ is defined as:

$$\frac{1}{r}\frac{\partial \psi}{\partial r} = u_z - U_{bubb}, \quad \frac{1}{r}\frac{\partial \psi}{\partial z} = -u_r, \tag{8}$$

where U_{bubb} is the velocity of the moving bubble. As illustrated in Fig. 1, a large anti-clockwise circulation is found inside the gas phase between smaller clockwise circulations in the front and rear of a gas bubble. The circulation can also be found in the liquid region. The present result agrees with the sketch by Taylor (1961) and the visualization by Thulasidas et al. (1997).

In Fig. 3, the void fraction ϵ is plotted against the volumetric gas flow ratio β_g. The relationship is given by:

$$\beta_g = \frac{j_g^*}{j_g^* + j_l^*} = \epsilon \frac{U_{bubb}^*}{U_{TP}^*}. \tag{9}$$

The experimental results by Hayashi et al. (2007) are also shown for comparison. Generally, both experimental and numerical results agree well with the so-called Armand correlation (Armand and Treschev, 1946), which is proposed

for conventional macro-sized tubes as:

$$\epsilon = 0.833\beta_g. \tag{10}$$

By combining Eqs. (9) and (10), we obtain:

$$\frac{U^*_{bubb}}{U^*_{TP}} = 1.2, \tag{11}$$

which implies that the bubble velocity is about 1.2 times larger than the two-phase mean velocity. This is because a gas slug flows around the central part of a tube.

3.2 Temperature Field

Temperature profiles at different Re_{TP} are shown in Figs. 4 a)-c). The top figure shows the wall temperature distribution, while the bottom the temperature distributions in the whole computational domain. The void fraction is kept constant as $\epsilon = 0.3$. The dimensionless temperature $\theta(r, z)$ is defined as:

$$\theta(r, z) = \frac{T(r, z) - \langle T_{wall} \rangle}{\langle T_{wall} \rangle - \langle T_m \rangle}, \tag{12}$$

where $\langle T_m \rangle$ and $\langle T_{wall} \rangle$ denote the domain-averaged bulk and wall temperatures, respectively. The bulk mean temperature $\langle \Theta_m \rangle$ is defined over the whole domain as:

$$\langle \Theta_m \rangle = \frac{\int_0^{L_z} \int_0^R \rho u_z C_p \theta(r, z) dr dz}{\int_0^{L_z} \int_0^R \rho u_z C_p dr dz}. \tag{13}$$

Accordingly, the averaged dimensionless wall temperature is $\langle \Theta_{wall} \rangle = 0$.

Note that since we impose a constant heat flux condition at the wall, the bulk temperature increases linearly in the axial direction. In Fig. 4, the bulk temperature is subtracted in order to focus on the temperature fluctuation.

The two-phase Nusselt number Nu_{TP} in each case is also shown in Fig. 4. Here, Nu_{TP} is defined as:

$$Nu_{TP} = \frac{h^*_{TP} D^*}{\lambda^*_l} = -\frac{2(\partial\theta/\partial r)_{wall}}{\langle\Theta_m\rangle}. \tag{14}$$

At a low Re_{TP} of 32, the thermal diffusion surpasses the convective heat transfer. Due to the much smaller thermal capacity of gas, the temperature in the gas phase is higher than that in liquid phase. The highest temperature in the whole domain locates at the rear of a gas bubble. This phenomenon agrees with the experimental observation by Monde and Mitsutake (1995), who measured the wall temperature fluctuations at different streamwise positions in mini channels and reported the temperature jump associated with the passage of a gas bubble. Similar results have also been reported by Fukagata et al. (2007). In the liquid slug region, the bulk temperature increases along the flow direction. Under this condition, the heat transfer characteristics are essentially the same as that in the thermally developing region of a single-phase flow.

As Re_{TP} increases, the convection plays a more important role. Consequently, the temperature profile inside a liquid slug converges to the profile of the streamline shown in Fig. 1, which is the solution of the temperature field in the limit of $Pe_T \to \infty$. At high Reynolds numbers of $Re_{TP} = 390$ and 760, the wall temperature fluctuation almost vanishes. This suggests that the thermal resistance inside an adherent liquid film between the slug and the wall becomes dominant.

A dividing streamline, which is depicted by a broken line close to a wall in Fig. 1 indicates that there exists no fluid exchange across this boundary. Therefore, it is possible to decompose the whole flow field into an adherent liquid film and the outer region, i.e., the gas-liquid slug region. The results in Fig. 4 suggest that the thermal coupling between the two regions is particularly important in predicting the overall heat transfer.

4 Heat Transfer Modelling

4.1 Basic assumptions

The present heat transfer model is schematically shown in Figs. 5 a, b). The whole domain is modelled as an adherent liquid film with alternately passing gas and liquid slugs (see, Fig. 5 a)). The adherent film was referred to as a lubricating film by Kreutzer et al. (2005), and it spans beneath both the gas and liquid slugs. For simplicity, both gas and liquid slugs are modelled as cylinders with radius of $R_{slug} = R - \delta$. We assume that the liquid film is stagnant and its thickness δ is constant along the wall. We have confirmed that these assumptions are reasonable for all flow conditions considered here. Due to the no-slip condition at the wall, we assume that the velocity inside the adherent film is negligible so that all gas and liquid injected into the micro tube is assumed to flow in the slug region, which is now defined as, $r < R_{slug}$. Therefore, the ratio of the gas and liquid slug lengths, i.e., L_{bubble} and L_{slug} in Fig. 5 a), is given by:

$$\frac{L_{bubble}}{L_{slug}} = \frac{\beta_g}{\beta_l}, \tag{15}$$

where β_l and β_g denote the volumetric flow fractions of liquid and gas, respectively. Obviously, $\beta_l + \beta_g = 1$, $0 \leq \beta_l \leq 1$ and $0 \leq \beta_g \leq 1$.

Since the heat capacity and conductivity of gas are negligible, while the liquid film thickness is sufficiently small, we model the overall heat transfer as a one-dimensional unsteady heat conduction inside the liquid film with a time-dependent heat transfer rate at the interface between the film and slug regions as illustrated in Fig. 5 b).

4.2 Formulation

Since $\delta \ll R$, we neglect the effect of the tube curvature inside the liquid film and the distance from the wall is denoted by y hereafter. This transient one-dimensional heat conduction problem in the y direction can be described as:

$$\frac{\partial T^*}{\partial t^*} = \alpha^* \frac{\partial^2 T^*}{\partial y^{*2}}. \tag{16}$$

Here, T^* and α^* are the temperature and the thermal diffusion coefficient in liquid. At the bottom wall, a constant heat flux condition is applied:

$$-\lambda^* \frac{\partial T^*}{\partial y^*} = q^* = const. \ \ at \ \ y^* = 0. \tag{17}$$

At the interface between the slug and film regions, a thermal boundary condition of the third kind is assumed:

$$-\lambda^* \frac{\partial T^*}{\partial y^*} = h_i^*(t) T^* \ \ at \ \ y^* = \delta^*. \tag{18}$$

Note that we shift the temperature so that the bulk temperature is zero so that T^* represents the temperature deviation form the bulk temperature. Here, h_i is the interfacial heat transfer rate from the liquid film to the slug region.

Considering that the heat capacity and conductivity of the gas phase are quite small, h_i should be negligible when a gas bubbule passes above the liquid film. In addition, assuming that the heat transfer rate h_{slug} of the liquid slug is uniform along the streamwise direction, $h_i(t)$ can be modelled as:

$$\begin{aligned} &h_i^*(t) = h_{slug}^*, \ \ 0 < t^* < t_l^*, \\ &h_i^*(t) = 0, \ \ t_l^* < t^* < t_p^*. \end{aligned} \tag{19}$$

Here, t_p^* is the entire period, while t_l^* is the duration in which the liquid slug passes above the liquid film. Hence, $t_p^* = t_l^* + t_g^*$, where t_g^* is the gas slug passage duration. In the slug region, we assume that the gas and liquid slugs travel at the same velocity. Therefore, t_l^* and t_g^* are given by L_{slug}^*/U_{TP}^* and L_{bubble}^*/U_{TP}^*, respectively. The time trace of h_i^* is schematically shown in Fig. 6. Now, the major task is to find how the total heat transfer rate h_{TP}^* from the bottom wall to the bulk fluid should be correlated with h_{slug}^*, t_l^*, t_g^* and δ^*.

4.3 Dimensionless parameters

The energy equation (16) are normalized as follows:

$$\frac{\partial T}{\partial t} = Fo\frac{\partial^2 T}{\partial y^2}, \tag{20}$$

where the temperature T, time t and distance from the bottom wall y are normalized by $\Delta T^* = q^*\delta^*/\lambda^*$, t_p^* and δ^*, respectively. The Fourier number is defined as $Fo = \alpha^* t_p^*/\delta^{*2}$.

Similarly, the boundary conditions of Eqs. (17) and (18) are respectively normalized as:

$$\frac{\partial T}{\partial y} = -1 \;\; at \;\; y = 0, \tag{21}$$

$$\frac{\partial T}{\partial y} = -B_i h_i(t) T \;\; at \;\; y = 1. \tag{22}$$

Here, B_i is the Biot number defined as $B_i = \overline{h_i}\delta^*/\lambda^*$ and h_i is normalized by its mean value as $h_i = h_i^*/\overline{h_i^*}$ so that:

$$\begin{aligned} h_i(t) &= \beta_l^{-1}, \;\; 0 < t < \beta_l, \\ h_i(t) &= 0, \;\; \beta_l < t < 1. \end{aligned} \tag{23}$$

Here, t_l^*/t_p^* is replaced with β_l, since we assume that the gas and liquid flow in the slug region is homogeneous.

From the above, the heat transfer rate is governed by the three dimensionless parameters, i.e., Bi, Fo and β_l.

4.4 Heat transfer model

4.4.1 Heat transfer rate

First, we consider the mean temperature profile inside a liquid film. Since there exists no heat source, the time-averaged temperature profile should be linear. Considering the boundary condition of Eq. (21), the mean temperature profile is given by:

$$\overline{T}(y) = \overline{T}(1) + (1 - y), \tag{24}$$

where the over-bar represents time-averaging. Equation (24) only gives us the relative temperature inside the liquid film. The mean temperature $\overline{T}(1)$ at the interface between the film and slug regions is determined as a result of the heat transfer from the liquid film to the bulk.

By applying time-averaging to Eq. (22), the following condition for $\overline{T}(1)$ is obtained:

$$\frac{d\overline{T}}{dy} = -1 = -B_i\overline{h_i \cdot T(1)} = -B_i\{\overline{h_i} \cdot \overline{T}(1) + \overline{h_i' \cdot T'(1)}\}. \tag{25}$$

Since $\overline{h_i} = 1$, the interfacial mean temperature $\overline{T}(1)$ is obtained from Eq. (25) as:

$$\overline{T}(1) = {B_i}^{-1} - \overline{h_i' \cdot T'(1)}. \tag{26}$$

Substituting Eq. (26) into Eq. (24), the mean bottom temperature $\overline{T}(0)$ is obtained as:

$$\overline{T}(0) = {B_i}^{-1} - \overline{h_i' \cdot T'(1)} + 1. \tag{27}$$

The overall heat transfer rate h_{TP} from the bottom wall to the bulk is calculated as:

$$h_{TP} = \frac{q}{\overline{T}(0)} = Fo\Big[\{{B_i}^{-1} - \overline{h_i' \cdot T'(1)}\} + 1\Big]^{-1}. \tag{28}$$

Consequently, the Nusselt number Nu_f of the liquid film becomes:

$$Nu_f = \frac{h_{TP}}{Fo} = \Big[\{{B_i}^{-1} - \overline{h_i' \cdot T'(1)}\} + 1\Big]^{-1}. \tag{29}$$

The above result suggests that Nu_f is determined as a result of two thermal resistances in the slug and film regions, which appear as the first and second terms in the square bracket on the right hand side of Eq. (29), respectively. In addition, the first term, i.e., the thermal resistance inside the slug region, includes the correlation between the fluctuations of the heat transfer rate h_i and the interfacial temperature $T(1)$. If we neglect the correlation term, Eq. (29) reduces to:

$$Nu_{f_0} = ({B_i}^{-1} + 1)^{-1}. \tag{30}$$

The above model is referred to as "crude model" and the prediction by this model is denoted by Nu_{f_0}. Note that Nu_{f_0} is solely a sum of two mean thermal resistances in the slug and film regions, which appear in the first and second terms in Eq. (30).

In order to show the significance of the correlation $\overline{h_i' \cdot T'(1)}$ in Eq. (29), we numerically solve the one-dimensional heat conduction equation (21) under the boundary conditions of Eqs. (21) and (22) with systematically changing

the dimensionless parameters in the range of $0.1 \leq B_i \leq 10$, $0.1 \leq Fo \leq 10$ and $0.1 \leq \beta_l \leq 0.9$, respectively.

The comparison between the numerical solutions Nu_f and the crude-model predictions Nu_{f_0} is shown in Fig. 7. It is found that the neglect of $\overline{h_i' \cdot T'(1)}$ results in significant overestimate of Nu_f.

4.4.2 Two-layer heat conduction model

The results in the previous subsection suggest that the correlation $\overline{h_i' \cdot T'(1)}$ should be appropriately taken into account in order to predict the overall heat transfer. However, due to the coupling of two fluctuating quantities of h_i and $T(1)$ appearing in Eq. (22), the analytical expression of thermal transient behavior inside the film is difficult to obtain, and even if it is possible, the resultant solution usually becomes too complicated to be used in real applications. Therefore, in this section, we derive an approximate solution based on a simple two-layer heat conduction model.

Before going into the details, a typical numerical result of transient thermal behavior inside the liquid film at $Fo = 0.25$, $B_i = 1.0$ and $\beta_l = 0.5$ is shown in Fig. 8. It is observed that the temperature fluctuation mainly occurs in the near-interface region, i.e., $1 - \eta_t \leq y \leq 1$, while the temperature is almost steady in the outer region, i.e., $0 \leq y \leq 1 - \eta_t$. Here, the thermal penetration thickness η_t can be estimated by the liquid-slug passage time β_l and the dimensionless conductivity Fo as $\eta_t \sim \sqrt{Fo\beta_l}$.

In view of the above result, we divide the liquid film into two layers. In the first layer adjacent to the interface, the temperature temporally fluctuates in response to h_i. In the second layer, the temperature is assumed to be steady and its profile is given by Eq. (24). Obviously, estimating the temperature fluctuation in the first layer is essential. To the first approximation, we assume

the temperature profile T_1 inside the first layer is uniform in the y direction so that T_1 is solely a function of time. We can derive a macroscopic energy balance in the first layer as:

$$\eta_t \frac{dT_1}{dt} = Fo(1 - B_i h_i T_1), \tag{31}$$

where the first term on the right-hand-side represents heating from the bottom, i.e., the interface between the first and second layer, while the second term corresponds to the cooling at $y = 1$ due to the passage of a liquid slug above the film.

During the liquid slug passage period, i.e, $0 < t < \beta_l$, the interfacial heat transfer rate is constant as $h_i = \beta_l^{-1}$ according to Eq. (23). Therefore, the analytical solution of T_1 is obtained as:

$$T_1(t) = C\exp(-\frac{B_i Fo}{\beta_l \eta_t} t) + \frac{\beta_l}{B_i} \quad at \;\; 0 < t < \beta_l. \tag{32}$$

Similarly, during the gas passage period, i.e., $\beta_l < t < 1$, h_i becomes zero. Therefore,

$$T_1(t) = C\exp(-\frac{B_i Fo}{\eta_t}) + \frac{\beta_l}{B_i} + \frac{Fo}{\eta_t}(t - \beta_l) \quad at \;\; \beta_l < t < 1. \tag{33}$$

Since we consider a fully developed thermal field, the proportional coefficient C is determined so as to satisfy a temporally-periodic condition, namely, $T_1(0) = T_1(1)$, as:

$$C = \frac{Fo(1 - \beta_l)}{\eta_t\{1 - \exp(-\frac{B_i Fo}{\eta_t})\}}. \tag{34}$$

From Eqs. (32-34), the mean interfacial temperature is calculated as:

$$\overline{T_1} = \overline{T}(1) = \frac{1 - \beta_g^2}{B_i} + \frac{Fo\beta_g^2}{\eta_t}\Big\{\frac{1}{1 - \exp(-\frac{B_i Fo}{\eta_t})} - \frac{1}{2}\Big\}. \tag{35}$$

Substituting into Eq. (24), the bottom wall temperature is obtained by $\overline{T}(0) = \overline{T}(1) + 1$. Eventually, the Nusselt number Nu_{f_model} predicted in the present two-layer model is given by:

$$Nu_{f\_model} = \frac{1}{\overline{T}(0)} = \left[\frac{1-\beta_g^2}{B_i} + \frac{Fo\beta_g^2}{\eta_t} \left\{ \frac{1}{1-\exp(-\frac{B_i Fo}{\eta_t})} - \frac{1}{2} \right\} + 1 \right]^{-1}. \quad (36)$$

Here, we briefly remark on the thermal penetration length η_t. As we discussed above, η_t is estimated as $\eta_t = \alpha\sqrt{Fo\beta_l}$, where α is an arbitrary constant in the order of 1. Since η_t can not exceed the liquid film thickness, η_t is defined as:

$$\eta_t = \mathrm{Min}(\alpha\sqrt{Fo\beta_l}\ ,\ \ 1). \quad (37)$$

We confirm that $\alpha = 0.55$ provides the best fit to the numerical data. The comparison between the numerical solutions Nu_f and the model predictions Nu_{f_model} over the prescribed ranges of Fo, B_i and β_l is shown in Fig. 9.

The present model (36) reduces to the crude model (30) when $Fo/\eta_t \ll 1$ and $B_i \ll (Fo/\eta_t)^{-1}$. The ratio Nu_{f_model}/Nu_{f_0} of the predictions by the present and crude models at the volumetric liquid ratio of $\beta_l = 0.5$ is shown in Fig. 10. In accordance with the above consideration, when $Fo \ll 1.0$, Nu_{f_model}/Nu_{f_0} is almost equal to 1.0, indicating that the crude model (30) provides good prediction. On the other hand, when Fo is larger than 1, the contribution of $\overline{h_i' \cdot T'(1)}$ in Eq. (29) becomes important so that Nu_{f_model}/Nu_{f_0} significantly deviates from 1.0. In such cases, the present model (36) needs to be used instead of the crude model (30).

5 Model Verification

5.1 Heat transfer model for gas-liquid slug flow

The Nusselt number Nu_{TP} of gas-liquid slug flow can be related to Nu_f as:

$$Nu_{TP} = \frac{h^*_{TP} D^*}{\lambda^*_l} = Nu_f(B_i, Fo, \beta_l)\left(\frac{\delta^*}{D^*}\right)^{-1}. \tag{38}$$

where D^* is a tube diameter. In real experiments, the volumetric liquid flow ratio β_l is usually given. Hence, the remaining parameters are B_i, Fo and the dimensionless film thickness δ^*/D^*. In order to determine the three parameters, the heat transfer rate h^*_{slug} in the liquid slug region and the film thickness δ^* need to be predicted. In the following subsections, we will discuss modelling of these quantities.

5.2 Heat transfer rate in liquid slug

As discussed in the next subsection, the liquid film thickness is generally much thinner than the tube diameter so that it is negligible in the liquid slug region. In addition, the surface tension is so strong that the shapes of a gas bubble at the front and rear parts are kept almost spherical in all cases considered. Therefore, that the change of the surface tension should not significantly influence the dynamics of a circulation inside a liquid slug.

The remaining parameters govern the flow field inside the liquid slug are the Reynolds number Re_{TP} and the liquid slug length L_{slug}. Therefore, the heat transfer in liquid slug should be determined by the following dimensionless parameters.

$$Nu_{slug} = \frac{h^*_{slug} D^*}{\lambda^*_l} = f(Re_{TP}, L_{slug}, Pr_l), \tag{39}$$

Here, we remark on the Reynolds number effect. As shown in Fig. 2, the velocity profile at the center of liquid slug is almost identical to the parabolic profile of the single-phase laminar flow, which is independent of the Reynolds number. Actually, we have confirmed that the flow field in the liquid slug is hardly influenced by Re_{TP} under a wide rage of Re_{TP} from $Re_{TP} = 32$ to 720. Therefore, the Reynolds number effect on the velocity field is considered to be minor as far as the flow is laminar. Hence, Eq. (39) is further simplified as:

$$Nu_{slug} = f(Pe_l, L_{slug}). \tag{40}$$

In the present study, we have carried out numerical simulations with systematically changing Pe_l and L_{slug} as $100 < Pe_l < 6000$ and $1 < L_{slug} < 7$, and obtain the correlation for Nu_{slug} by fitting these data. It is expressed as:

$$Nu_{slug} = \frac{h^*_{slug} D^*}{\lambda^*_l} = 24.2 + 0.54 Pe_l^{0.45} (L^*_{slug}/D^*)^{-1.34}. \tag{41}$$

Good agreement between the numerical results and Eq. (41) is confirmed in Fig. 11.

5.3 Liquid film thickness

Bretherton (1961) first applied a lubrication theory in order to predict the shape of the liquid film formed between the spherical bubble front and the flat film in the far downstream. In his analysis, the inertial force was neglected due to high viscosity of fluid. As a result, the film thickness is determined by the Capillary number Ca as:

$$\frac{\delta^*}{D^*} = 0.67 Ca^{2/3}, \quad \text{where} \quad Ca = \frac{\mu^*_l U^*_{bubble}}{\sigma^*}. \tag{42}$$

Recently, Han and Shikazono (2008) carried out systematic measurement of the liquid film thickness formed behind a moving liquid slug in micro tubes by

employing a laser confocal technique. They show that the experimental results agree well with Eq. (42) at small Ca, while Eq. (42) underestimates the film thickness when $Ca > 0.02$ due to the inertia effect.

In Fig. 12, Eq. (42), the experimental data of Han and Shikazono (2008) and the present numerical data are plotted. It should be noted that at least 6 grid points generally exist inside the liquid film in the present calculations. We confirmed that doubling the radial grid number causes only 2% difference in the film thickness. It is found that the present numerical results show significant deviations from both Eq. (42) and the experimental data at low Ca. The possible reason for this discrepancy is difference in the bubble length. A closer look at the experimental data reveals that the film thickness is increased when the bubble length is small, i.e., $L_{bubble}/R < 6$. Similar trend is also observed in the present numerical data. When the bubble length is short, the interaction between the bubble front and rear becomes important. This may cause an increase in the film thickness.

Although it might be possible to develop a new correlation for the film thickness by taking into account the bubble length, it is out of the scope of the present study. Instead, we employ a rather simple model proposed by Suo and Griffith (1964). In their model, it is assumed that the liquid film with thickness of δ^* is stagnant, while the gas and liquid slug travels at the same speed over the film. Therefore, the effective tube radius is reduced to $R^* - \delta^*$. This causes the difference between U^*_{TP} and U^*_{bubble} so that:

$$\left(1 - \frac{\delta^*}{R^*}\right)^2 = \frac{U^*_{TP}}{U^*_{bubb}} = \frac{\epsilon}{\beta_g}. \tag{43}$$

By using the Armand correlation (10), the film thickness is estimated as:

$$\frac{\delta^*}{R^*} = 0.087. \tag{44}$$

Although this model cannot predict the Capillary number effect on the film thickness, it predicts the present numerical data fairly well as shown in Fig. 12.

5.4 Comparison with numerical results

By substituting Eqs. (41) and (44) into Eq. (38), we can finally predict Nu_{TP}. The comparison between the model predictions and the present numerical results is shown with solid circles in Fig. 13. The predictions by the crude model of Eq. (30) are also plotted by open circles for comparison.

The Nusselt number obtained in the present simulation varies from 2.85 to 10.25 depending on the flow pattern. This is in contrast with the single phase flow, in which the the Nusselt numbe is constant, i.e., Nu = 4.36 under a constant heat flux condition, regardless of the Reynolds and Prandtl numbers.

In accordance with the analyses in the previous section, the crude model generally overestimates Nu_{TP} due to the neglect of the correlation term in Eq. (29). It is, however, removed by employing the present model. It was indicated that the thermal coupling between the slug and film regions have to be appropriately taken into account in order to predict the heat transfer rate in a gas-liquid slug flow.

It is confirmed that the present model still has a error of around 25 %. This scattering is attributed to the errors in predicting h^*_{slug} and δ^* by Eqs. (41) and (44). More sophisticated models are necessary to improve the prediction. Nonetheless, we demonstrated that the importance of the thermal coupling between the liquid film and slug regions, and presented its appropriate modelling.

6 CONCLUSIONS

We conducted a series of numerical simulations of gas-liquid slug flows and associated heat transfer without phase change in a micro tube. It is found that the Nusselt number strongly depends on the flow pattern, and is up to 2.4 times higher than that of the single-phase laminar flow. This indicates that the gas-liquid slug flow without phase change is promising for heat transfer enhancement in practical applications.

The streamline function in the entire flow domain shows that the gas-liquid slug flow is generally characterized by an adherent liquid film with alternate passage of gas and liquid slugs above the film. In order to predict the effects of the flow pattern on the heat transfer, we model the overall heat transfer as one-dimensional unsteady heat conduction inside the liquid film with a time-dependent heat transfer rate between the film and slug regions.

Detailed analyses of the above one-dimensional model reveal that the overall heat transfer rate depends on not only respective mean thermal resistances in the film and slug regions, but the correlation between the fluctuations of the heat transfer rate and temperature at the interface between the liquid film and slug regions. In the present study, we first proposed a heat transfer model which takes into account the correlation, and verify it with the present numerical results over wide ranges of the slug length and the flow rate of each of gas and liquid.

The present model prediction can be further improved by elaborating the models for the liquid film thickness and the heat transfer rate in the liquid slug. From a practical point of view, the present model is useful in optimizing the flow pattern so as to achieve the highest heat transfer performance with the minimum pressure penalty. A phenomenological model for the pressure drop has been also proposed by He and Kasagi (2008b). Combining such a

pressure drop model with the present heat transfer model is promising for the optimization of the flow pattern. These remain to be future work.

ACKNOWLEDGMENT

The authors are grateful to Professors Y. Suzuki and N. Shikazono for their fruitful discussions, and also Dr. Y. Han for providing his valuable experimental data.

Roman symbols

C	concentration
Cn	Cahn number, ϵ/R
C_p	thermal capacity, [J/kg K]
Ca	Capillary number, $\eta_L U/\sigma$
D	tube diameter, [m]
f	chemical potential
G	volumetric flux, [m^2/s]
h	heat transfer coefficient, [W/K m^2]
j	superficial velocity, [m/s]
L	longitudinal length, [m]
$\mathcal{M}$	dimensionless mobility
Nu	Nusselt number
p	pressure, [Pa]
Pe_C	concentration Peclet number,$UD/(\mathcal{M}\mu_L)$
Pe_l	thermal Peclet number,$\rho_L U C_{pL} D/\lambda_L$
Pr	Prandtl number

q	heat flux, [W/m^2]
r	radial direction, [m]
R	tube radius, [m]
Re	Reynolds number, $\rho_L U D/\eta_L$
t	time, [s]
T	temperature, [K]
$\vec{u}$	velocity
We	Weber number, $\rho_L U^2 D/\sigma$
U	mean velocity, [m/s]
z	longitudinal direction, [m]

α thermal diffusion coefficient [m^2/s]

β volumetric flow ratio

δ residual film thickness, [m]

η_ϵ interface thickness parameter

ϵ void fraction

σ surface tension coefficient, [N/m]

μ viscosity, [Pa s]

ν kinematic viscosity, [m^2/s]

λ thermal conductivity, [W/m K]

Ψ dimensionless bulk free energy

ψ dimensionless stream function

ρ density,[kg/m^3]

θ dimensionless temperature

Θ dimensionless mean temperature

Subscripts

$bubble$	gas bubble
$film$	residual film
g	gas phase
i	interface between a liquid film and slug regions
l	liquid phase
m	bulk mean
$slug$	gas/liquid slug region
TP	two-phase
$wall$	wall
z	longitudinal

Operator

$\langle\cdot\rangle$	domain average
$\bar{\cdot}$	time average

References

[1] Anderson, D.M., McFadden, G.B. and Wheeler, A.A., 1998. Diffuse-interface methods in fluids mechanics, *Annu. Rev. Fluid Mech.*, 30, 139–165.

[2] Armand, A.A. and Treschev, G.G., 1946. The resistance during the movement

of a two-phase systems in horizontal pipe. *Izv, Vses, Teplotek. Inst.*, 1, 16-23.

[3] Bretherton, F.P., 1961. The motion of long bubbles in tubes. *J. Fluid Mech.*, 10, 166–188.

[4] Fukagata, K., Kasagi, N., Ua-arayaporn, P. and Himeno, T., 2007. Numerical simulation of gas-liquid two-phase flow and convective heat transfer in a micro tube, *Int. J. Heat Fluid Flow*, 27, 72–82.

[5] Ghiaasiaan, S.M. and Abdel-khalik, S.I., 2001. Two-phase flow in microchannel. *Adv. Heat Transfer*, 34, 145–254.

[6] Han, Y.B. and Shikazono, N., 2008. Thickness of liquid film formed in slug flow in micro tube. *Proc. ECI Conf. on Heat Transfer and Fluid Flow in Microscale*, Hilton Whistler, Canada, Sep. 21-26.

[7] Hayashi, S., Kasagi, N. and Suzuki, Y., 2007. The effects of inlet flow conditions on gas-liquid two-phase flow in a micro tube, *Proc. HT2007 & 2007 ASME-JSME Thermal Engineering Summer Heat Transfer Conference*, Paper No. HT2007-32916, July 8-12, Vancouver, Canada.

[8] He, Q. and Kasagi, N., 2008a. Phase-Field simulation of small capillary-number two-phase flow in a microtube, *Fluid Dyn. Res.*, 40, 497–509.

[9] He, Q. and Kasagi, N., 2008b. Numerical investigation on flow pattern and pressure drop characteristics of slug flow in a micro tube, *Proc. 6^{th} Int. Conf. Nanochannel, Microchannel and Minichannel*, Jun. 23-25, Darmstadt, Germany.

[10] Jacqmin, D., 2000. Contact-line dynamics of a diffuse fluid interface, *J. Fluid. Mech.*, 402, 57–88.

[11] Kawaji, M., Mori, K. and Bolintineanu, 2009. The effects of inlet geometry and gas-liquid mixing on two-phase flow in microchannels, *ASME J. Fluids Engineering*, 131, 041302 1-7.

[12] Kawahara, A., Chung, P.M.-Y and Kawaji, M., 2002. Investigation of two-phase flow pattern, void fraction and pressure drop in a microchannel. *Int.*

J. Multiphase Flow, 28, 1411–1435.

[13] Kreutzer, M.T., Kapteijn, F., Moulijn, J.A. and Heiszwolf, J.J., 2005. Multiphase monolith reactors: Chemical reaction engineering of segmented flow in microchannels, *Chem. Eng. Sci*, 60, 5895–5916.

[14] Monde, M. and Mitsutake, Y., 1995. Enhancement of heat transfer due to bubbles passing through a narrow vertical rectangular channel (Change in heat transfer along flow), *Heat Mass Transfer*, 31, 77–82.

[15] Oliver, D.R. and Hoon, Y.A., 1968. Two-phase non-newtonian flow, *Trans. Inst. Chem. Eng.*, 46, 116–122.

[16] Serizawa, A., Feng, Z. and Kawara, Z., 2002. Two-phase flow in microchannels. *Experimental Thermal and Fluid Science*, **26**, 703–714.

[17] Suo, M. and Griffith, P., 1964. Two-phase flow in capillary tubes, *J. Basic Eng. ASME*, 86, 576–582.

[18] Taylor, G.I., 1961. Deposition of a viscous fluid on the wall of a tube, *J. Fluid Mech.*, 10, 1161–1165.

[19] Thome, J.R., Hajal, J.E. and Cavallini, A., 2003.Condensation in Horizontal Tubes, Part 1: Two-Phase Flow Pattern Map. *Int. J. Heat Mass Transfer*, 46(18):3349-3363.

[20] Thome, J.R., Hajal, J.E. and Cavallini, A., 2003.Condensation in Horizontal Tubes, Part 2: New Heat Transfer Model Based on Flow Regimes, *Int. J. Heat Mass Transfer*, 46(18):3365–3387.

[21] Triplett, K.A., Ghiaasiann, S.M., Abdel-Khalik, S.I. and Sadowski, D.L., 1999. Gas-liquid two-phase flow in microchannels. Part I: two-phase flow patterns. *International Journal of Multiphase Flow*, **24**, 377–394.

[22] Thulasidas, T.C., Abraham, M.A. and Cerro, R.L., 1997. Flow patterns in liquid slugs during bubble-train flow inside capillaries, *Chem. Eng. Sci.*, 52, 2947–2962.

Fig. 1 Bubble shape and relative streamlines at $\alpha = 0.29$ and $Re_{TP} = 288$. thick solid line: gas-liquid interface, thick broken line: dividing streamline between an adherent liquid film and gas-liquid slugs.

Fig. 2 Velocity profiles with different grid spacings at a) the front of a bubble and b) the center of slug.

Fig. 3 Relationship between the volumetric gas flow ratio β_g and void fraction ϵ.

Fig. 4 Temperature distributions at different Reynolds numbers Re_{TP} (top: wall temperature, bottom: counter plot in the whole computational domain) The temperature is normalized by the temperature difference between the wall and the bulk. The dotted line in the top figures represents the mean wall temperature, while the thick broken line in the bottom figures the interfacial location. a): $Re_{TP} = 32$, b): $Re_{TP} = 112$, c): $Re_{TP} = 390$.

Fig. 5 Conceptual figures of the present heat transfer model a) Decomposition of the entire flow field; b) Heat transfer modelling inside the adherent liquid film.

Fig. 6 Heat transfer rate at the interface between the liquid film and slug regions.

Fig. 7 Comparison between the Nusselt number Nu_f of the one-dimensional conduction problem and the prediction by the crude model (30)

Fig. 8 Transient behavior of temperature field in the liquid film at $Fo = 0.25$, $B_i = 1.0$ and $\beta_l = 0.5$.

Fig. 9 Comparison between the numerical solutions Nu_f and the model prediction Nu_{f_model}

Fig. 10 Ratio of the Nusselt numbers predicted by the present and crude models.

Fig. 11 Comparison between numerical solutions Nu_{slug} and the model prediction Eq. (41)

Fig. 12 Thickness of the adherent liquid film as a function of Ca.

Fig. 13 Comparison between the results of numerical simulation and the model predictions. Open circle: the crude model (30), Solid circle: the present model (36)

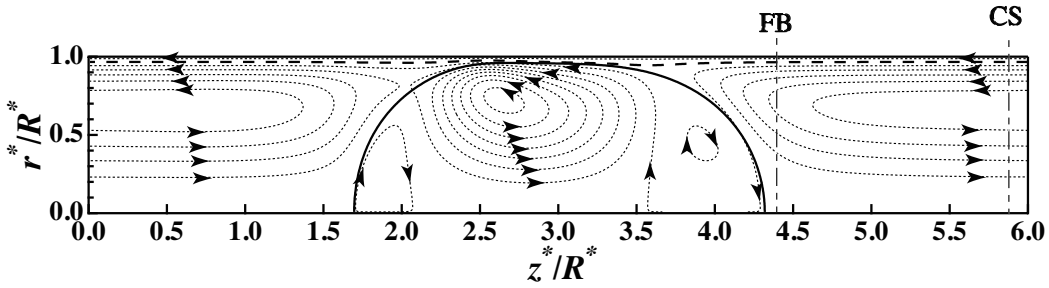

Fig. 1. Bubble shape and relative streamlines at $\epsilon = 0.29$ and $Re_{TP} = 288$. thick solid line: gas-liquid interface, thick broken line: dividing streamline between an adherent liquid film and gas-liquid slugs

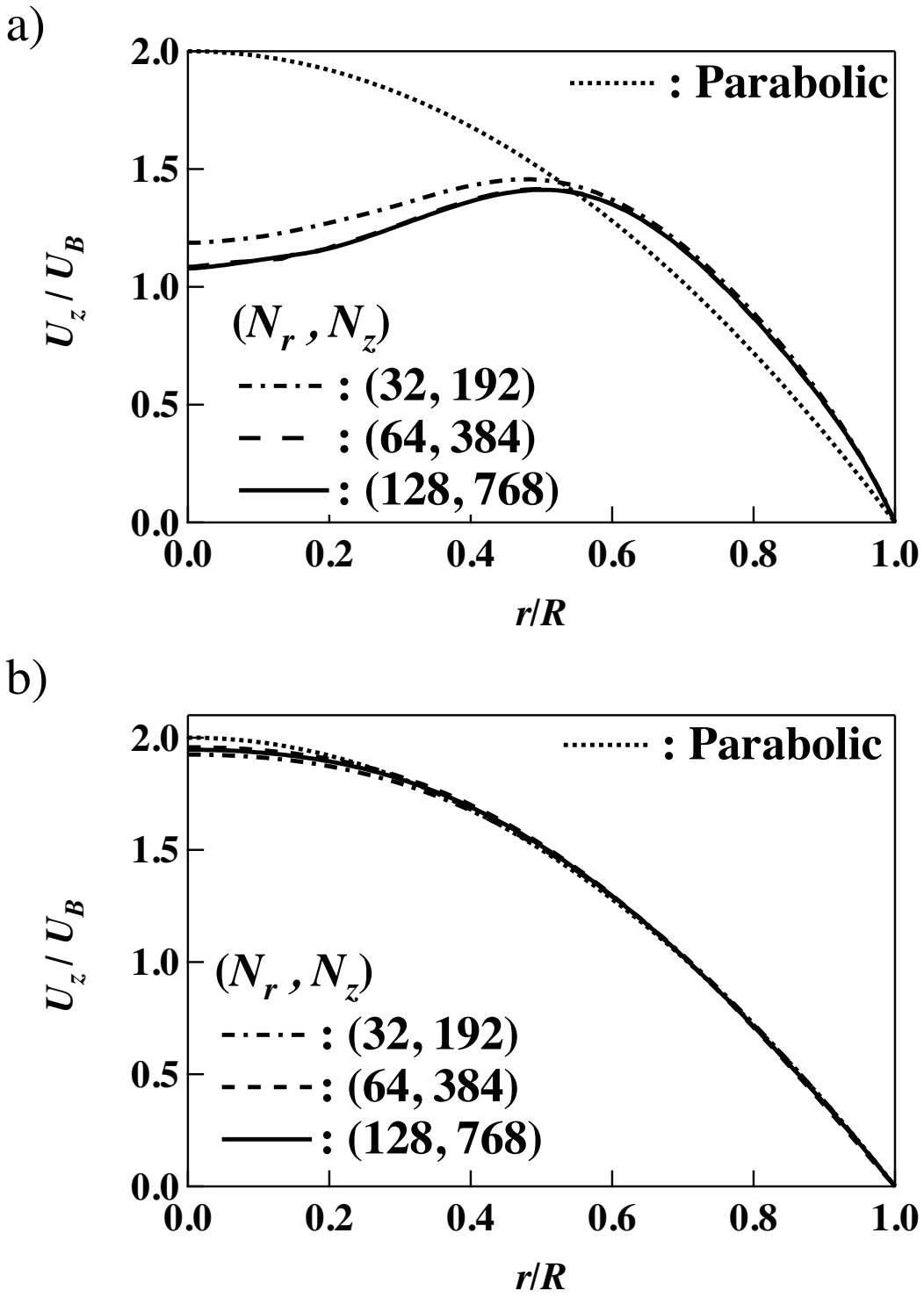

Fig. 2. Velocity profiles with different grid spacings at a) the front of a bubble and b) the center of slug

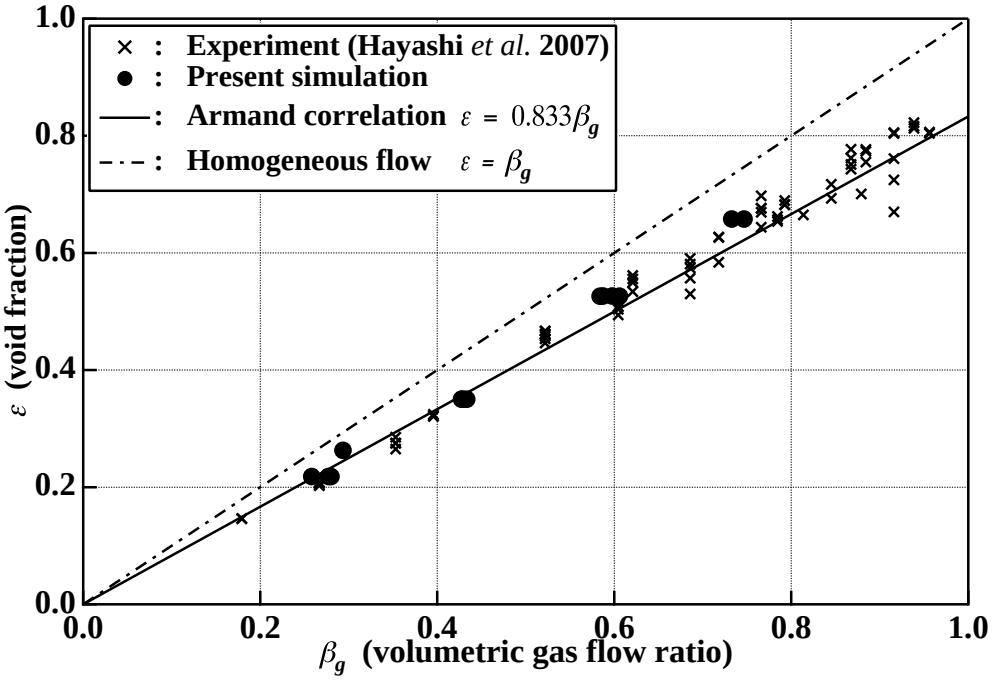

Fig. 3. Relationship between the volumetric gas flow ratio β_g and void fraction ϵ.

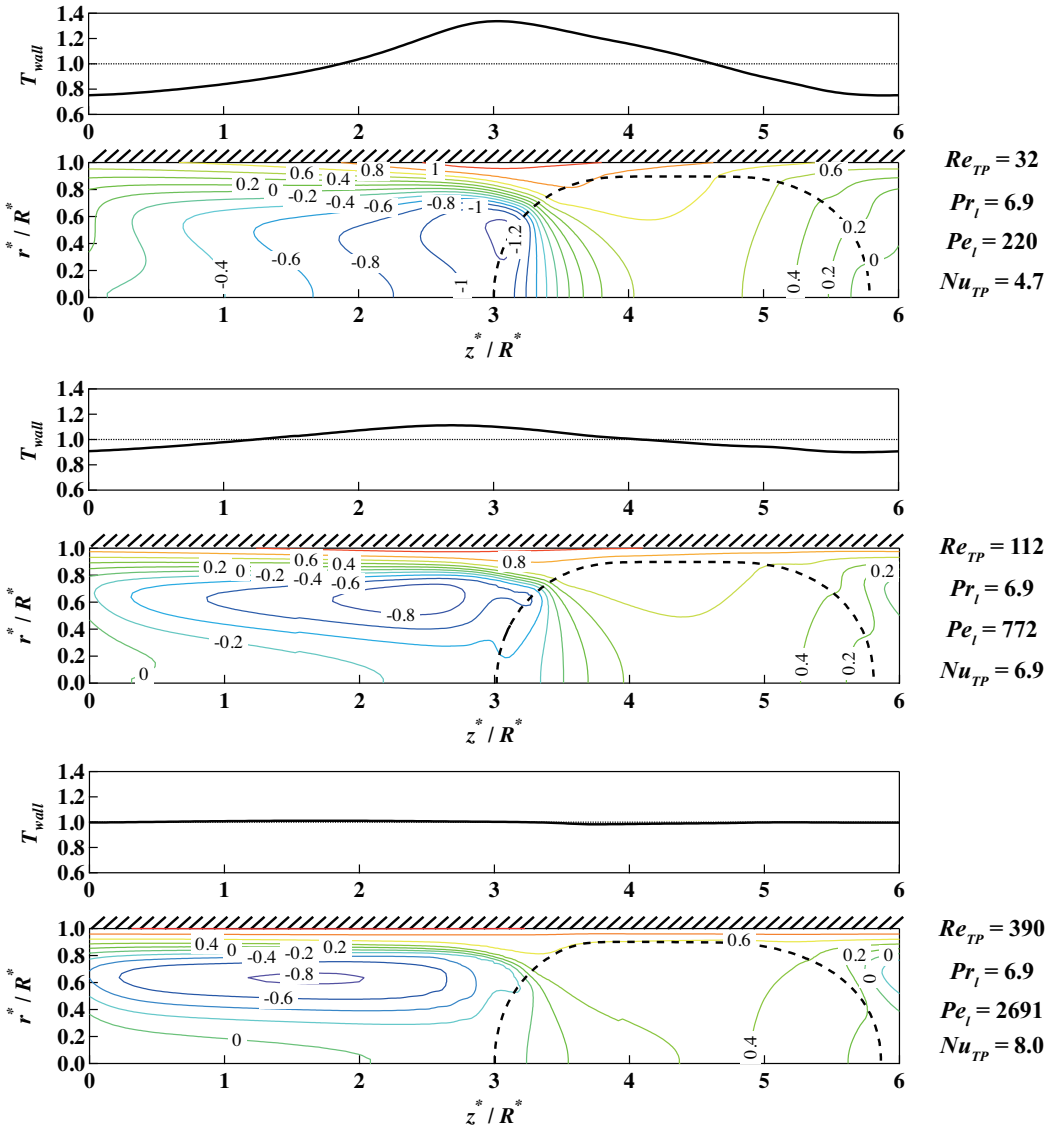

Fig. 4. Temperature distributions at different Reynolds numbers Re_{TP} (top: wall temperature, bottom: counter plot in the whole computational domain) The temperature is normalized by the temperature difference between the wall and the bulk. The dotted line in the top figures represents the mean wall temperature, while the thick broken line in the bottom figures the interfacial location. a): $Re_{TP} = 32$, b): $Re_{TP} = 112$, c): $Re_{TP} = 390$.

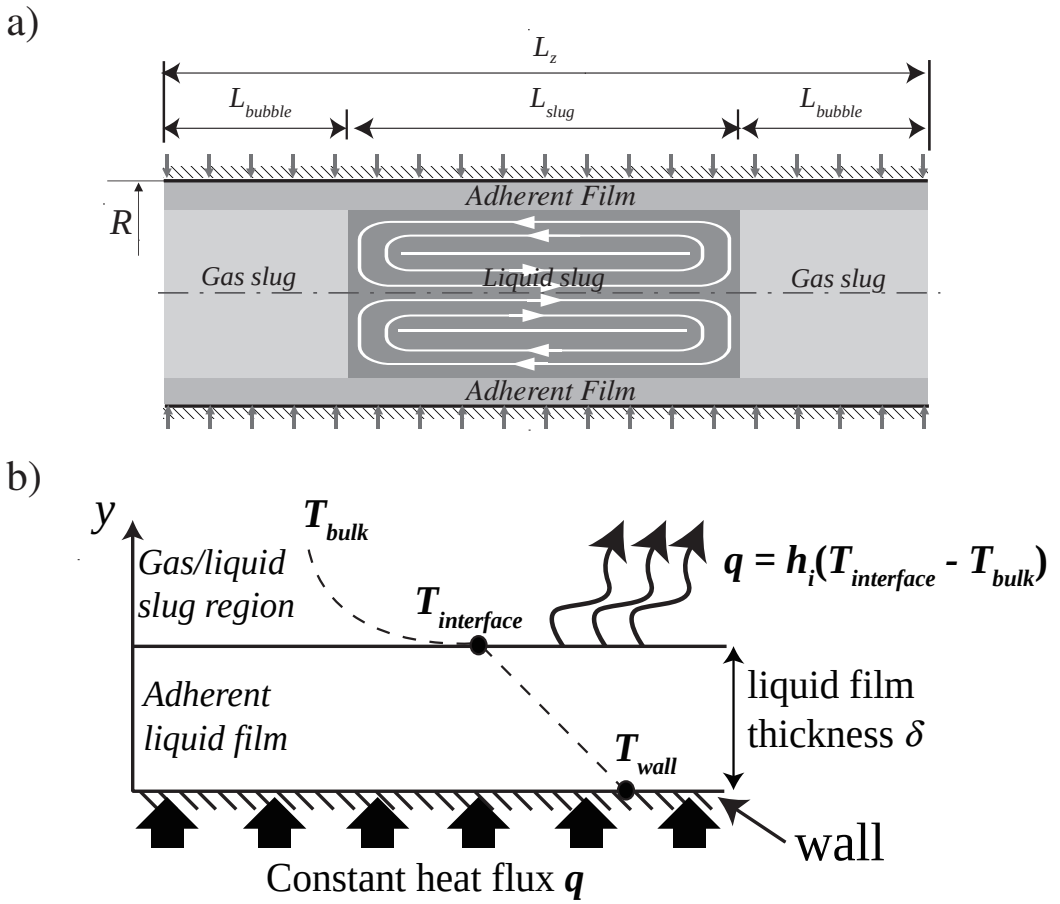

Fig. 5. Conceptual figures of the present heat transfer model a) Decomposition of the entire flow field; b) Heat transfer modelling inside the adherent liquid film.

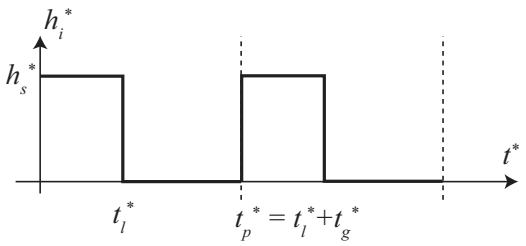

Fig. 6. Heat transfer rate at the interface between the liquid film and slug regions.

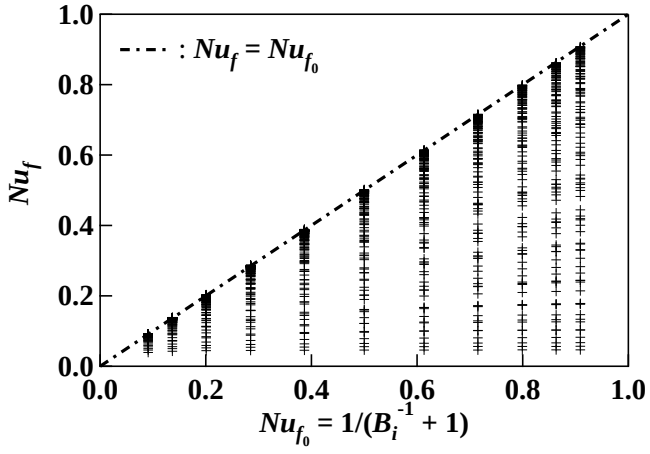

Fig. 7. Comparison between the Nusselt number Nu_f of the one-dimensional conduction problem and the prediction by the crude model (30)

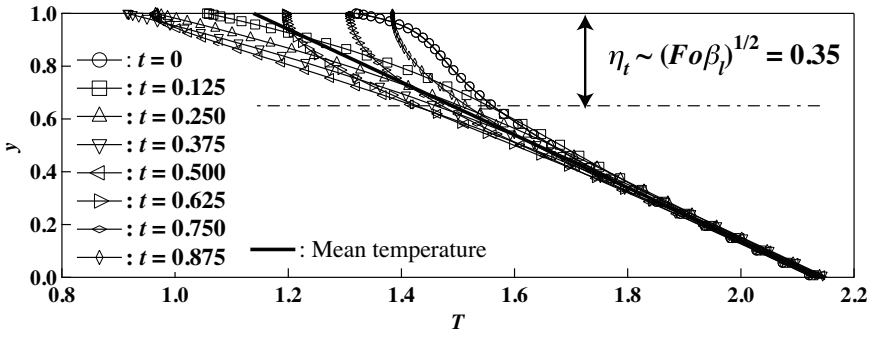

Fig. 8. Transient behavior of temperature field in the liquid film at $Fo = 0.25$, $B_i = 1.0$ and $\beta_l = 0.5$.

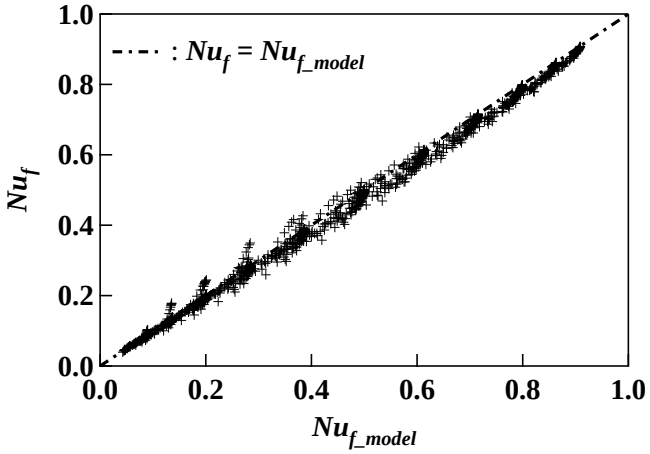

Fig. 9. Comparison between the numerical solutions Nu_f and the model predictions Nu_{f_model}

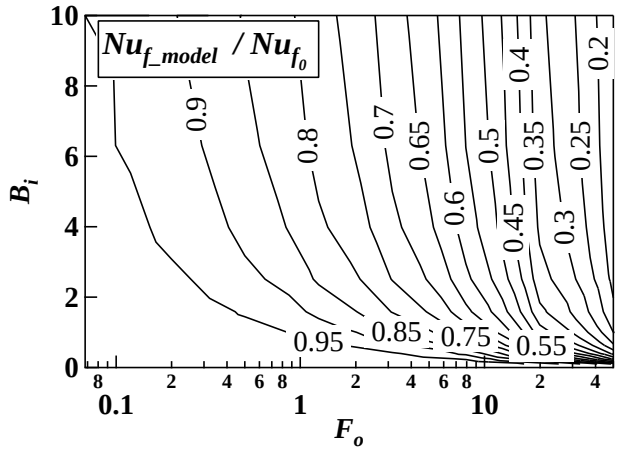

Fig. 10. Ratio of the Nusselt numbers predicted by the present and crude models.

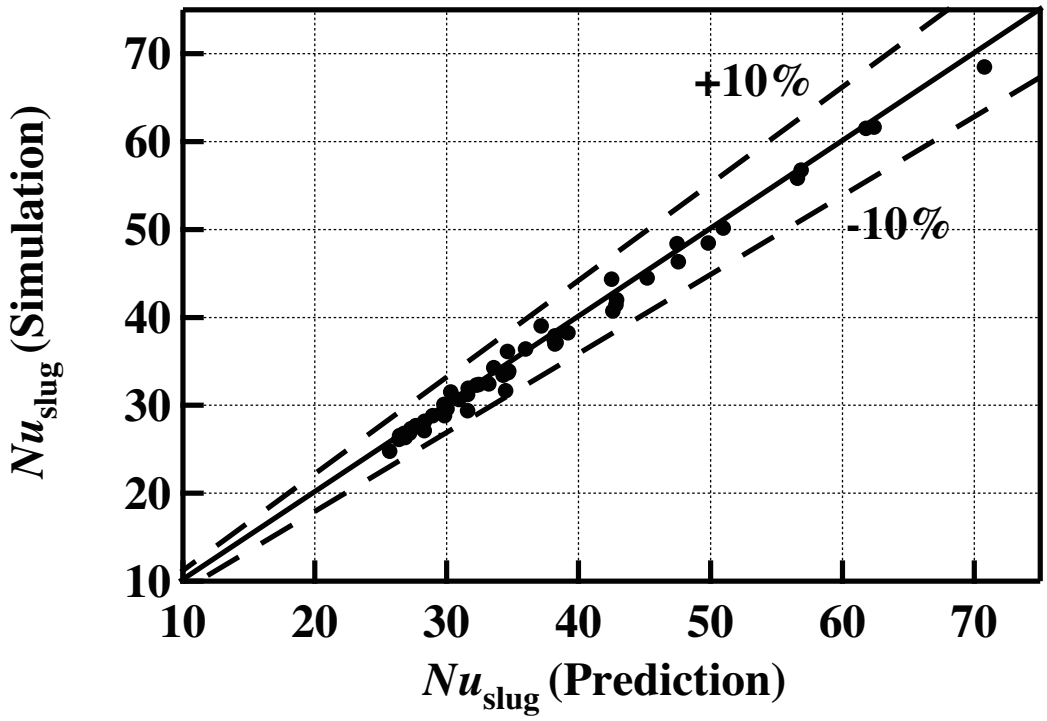

Fig. 11. Comparison between numerical solutions Nu_{slug} and the model prediction Eq. (41)

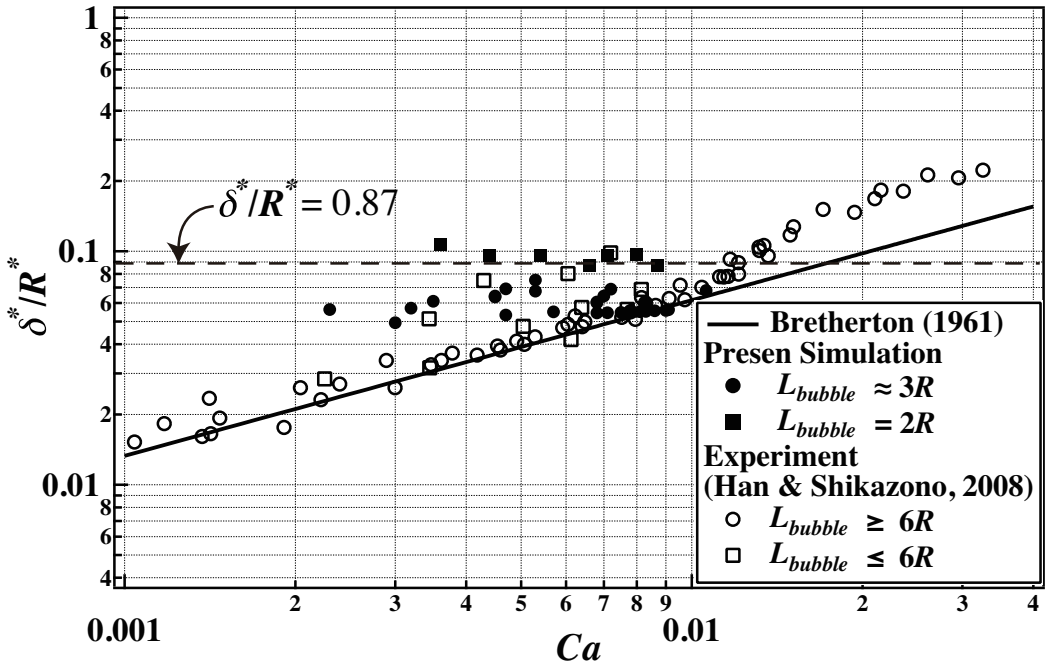

Fig. 12. Thickness of the adherent liquid film as a function of Ca.

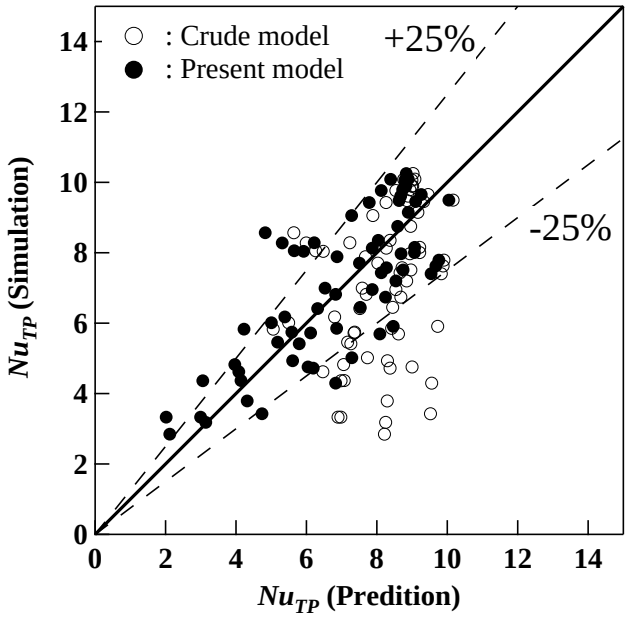

Fig. 13. Comparison between the results of numerical simulation and the model predictions. Open circle: the crude model (30), Solid circle: the present model (36)